



## PAPER

## Customizing the human-avatar mapping based on EEG error related potentials

## OPEN ACCESS

RECEIVED  
3 July 2023REVISED  
26 December 2023ACCEPTED FOR PUBLICATION  
26 January 2024PUBLISHED  
27 March 2024

Original Content from this work may be used under the terms of the [Creative Commons Attribution 4.0 licence](#).

Any further distribution of this work must maintain attribution to the author(s) and the title of the work, journal citation and DOI.



Fumiaki Iwane<sup>1,2,3,11,\*</sup> , Thibault Porssut<sup>4,5,10,11</sup> , Olaf Blanke<sup>5,6</sup> , Ricardo Chavarriaga<sup>7</sup> , José del R Millán<sup>2,3,8,9</sup> , Bruno Herbelin<sup>5,12,\*</sup> and Ronan Boulic<sup>4,12,\*</sup>

<sup>1</sup> Learning Algorithms and Systems Laboratory (LASA), École Polytechnique Fédérale de Lausanne (EPFL), 1015 Lausanne, Switzerland

<sup>2</sup> Dept. of Electrical and Computer Engineering, The University of Texas at Austin, Austin, TX 78712, United States of America

<sup>3</sup> Dept. of Neurology, The University of Texas at Austin, Austin, TX 78712, United States of America

<sup>4</sup> Immersive Interaction Research Group (IIG), Ecole Polytechnique Fédérale de Lausanne (EPFL), Lausanne, Switzerland

<sup>5</sup> Laboratory of Cognitive Neuroscience (LNCO), Ecole Polytechnique Fédérale de Lausanne (EPFL), Lausanne, Switzerland

<sup>6</sup> Dept. of Neurology, Geneva University Hospitals, Geneva, Switzerland

<sup>7</sup> Centre for Artificial Intelligence, Zurich University of Applied Sciences (ZHAW), Winterthur, Switzerland

<sup>8</sup> Dept. of Biomedical Engineering, The University of Texas at Austin, Austin, TX 78712, United States of America

<sup>9</sup> Mulva Clinic for the Neurosciences, The University of Texas at Austin, Austin, TX 78712, United States of America

<sup>10</sup> Capgemini Engineering, Paris, France

<sup>11</sup> These authors contributed equally to this work.

<sup>12</sup> These authors have equally supervised this work.

\* Author to whom any correspondence should be addressed.

E-mail: [fumi.iwane@nih.gov](mailto:fumi.iwane@nih.gov), [bruno.herbelin@epfl.ch](mailto:bruno.herbelin@epfl.ch) and [ronan.boulic@epfl.ch](mailto:ronan.boulic@epfl.ch)

**Keywords:** brain computer interface, virtual reality, EEG, error related potentials, break-in-embodiment, reinforcement learning

Supplementary material for this article is available [online](#)

## Abstract

**Objective.** A key challenge of virtual reality (VR) applications is to maintain a reliable human-avatar mapping. Users may lose the sense of controlling (sense of agency), owning (sense of body ownership), or being located (sense of self-location) inside the virtual body when they perceive erroneous interaction, i.e. a break-in-embodiment (BiE). However, the way to detect such an inadequate event is currently limited to questionnaires or spontaneous reports from users. The ability to implicitly detect BiE in real-time enables us to adjust human-avatar mapping without interruption. **Approach.** We propose and empirically demonstrate a novel brain computer interface (BCI) approach that monitors the occurrence of BiE based on the users' brain oscillatory activity in real-time to adjust the human-avatar mapping in VR. We collected EEG activity of 37 participants while they performed reaching movements with their avatar with different magnitude of distortion. **Main results.** Our BCI approach seamlessly predicts occurrence of BiE in varying magnitude of erroneous interaction. The mapping has been customized by BCI-reinforcement learning (RL) closed-loop system to prevent BiE from occurring. Furthermore, a non-personalized BCI decoder generalizes to new users, enabling 'Plug-and-Play' ErrP-based non-invasive BCI. The proposed VR system allows customization of human-avatar mapping without personalized BCI decoders or spontaneous reports. **Significance.** We anticipate that our newly developed VR-BCI can be useful to maintain an engaging avatar-based interaction and a compelling immersive experience while detecting when users notice a problem and seamlessly correcting it.

## 1. Introduction

Virtual reality (VR) systems are becoming widespread in industrial, clinical and training applications for their benefit in ecological validity and physical involvement of participants. One of the main challenges of VR is to provide users with a sense of

having a virtual body during immersion in order to interact with the virtual world. The sense of embodiment (SoE) for a virtual body representation, the avatar, is a highly subjective experience that must be induced and maintained to support successful interactions in immersive VR [1]. SoE has been described to involve the following components for successful

human-avatar mappings: agency, body ownership, and self-location [2]. The disruption of at least one of them causes a break in embodiment (BiE), leading to a degradation of the virtual experience [1, 3, 4]. However, the way to detect such an inadequate event is currently limited to explicit feedback from users, e.g. questionnaires or spontaneous reports. Detecting BiE implicitly and in real-time would allow customizing the mapping between users and their avatars so as to fine-tune the interaction possibilities in VR without interruption.

In the 1990s, research on neural processes revealed error-related brain activity in EEG signals originating from the anterior cingulate cortex (ACC) after perception of errors [5, 6]. Holroyd and Coles [7] proposed that an error-processing system in the ACC serves as reinforcement-learning signals to correct errors. Further studies have also shown that error-related potentials (ErrPs) spontaneously arise when users experience BiEs during avatar-based interaction in VR [4, 8–13]. These findings support the notion of an accumulation of errors in these conditions [14–16], where cognitive processes in embodiment contribute to a global error in user experience. It is also well established that brain–computer interfaces (BCIs) benefit from real-time ErrP detection to offer intuitive control of external devices without requiring explicit feedback, as instead they can infer participants' perception of errors from their brain activity and adapt accordingly [17–21]. Some BCIs have succeeded in decoding the presence of ErrPs during continuous interaction [22–24], with e.g. the possibility to customize robot trajectories for each participant based on continuous ErrP detection [25, 26]. It thus appears that the methods used in ErrP-based BCI provide the adequate approach for continuously and implicitly adjusting the interaction with avatar in immersive VR.

Although recent studies show that ErrP-based BCI allows customization of continuous human-computer interactions, its use is still limited to interactions with a computer application [24] or a robotic arm [25, 26]. This may in part be due to the need to train personalized decoders, which require a large amount of repetitions and observations before being operational. In our context, this limitation would, however, defeat the purpose of using BCI to implicitly improve interaction in VR as the objective is specifically to avoid repetitively causing BiE, and eventually to use this method in a general immersive VR application context. Hopefully, a recent study demonstrated the feasibility of using the non-personalized decoder with some reductions in decoding performance [23]. However, it remains to be tested if, despite these limitations, non-personalized ErrP decoders can be used in a different way, as in our case for adjusting the mapping between human and avatar actions.

In our previous study, we demonstrated the feasibility of adapting the human-avatar mapping in VR based on the explicit feedback of users [27]. However, it still needs to be demonstrated that it is possible to adjust this human-avatar mapping by implicitly predicting the occurrence of BiE, while avoiding to interrupt the interaction flow and break presence. We hypothesize that real-time detection of ErrPs during avatar-based interaction can predict the occurrence of BiE, and thus allows seamless customization of the mapping. To demonstrate this, we implemented a BCI system that monitors the presence (or absence) of ErrP in real time while distorting the human-avatar mapping in varying magnitudes (figures 1(a) and (c)).

The use of distortion of the human-avatar mapping has been frequently employed in 3D interaction methods, even without haptic feedback [28–30]. For example, one of the earliest methods focused on enhancing the effectiveness of user interactions by deliberately altering the mapping between real and virtual bodies for a stretching arm. This alteration resulted in an expanded reachable space centered around the user's body [31]. Nevertheless, the challenge lies in fine-tuning of distortion parameters while preventing the occurrence of BiE. For instance, Porssut *et al* [1, 32] demonstrated that users tolerate and even prefer distorted mapping with their avatar movement when this helps to accomplish complex movements. However, once distortion surpasses a certain threshold, it can lead to BiE. Specifically, our aim here was thus to customize the human-avatar mapping distortion magnitudes based on implicit ErrP-BCI feedback in order to aid in accomplishing a reaching action while preventing BiEs from occurring. We recorded EEG signals of participants while they were embodied in a full-body avatar. The participants performed reaching movements to a target while their avatar's reaching movement was distorted in varying magnitudes. We expect ErrPs to appear when participants perceive excessive support from the distortion. The real-time ErrP decoding output was used to identify optimal distortion magnitudes through a reinforcement learning (RL) algorithm. We then further investigated the feasibility of customizing the mapping with the non-personalized ErrP decoder outputs in addition to the use of personalized decoder in both time-locked and continuous classification.

## 2. Methods

### 2.1. Participants

37 healthy subjects participated in the study (36 right-handed, 16 females,  $23.4 \pm 3.5$  years [mean  $\pm$  std]). All participants had normal or corrected-to-normal vision and gave their informed consent prior to participation. The study was performed in accordance with the ethical standards as defined in the

Declaration of Helsinki and was approved by the Swiss Ethics Committees of the canton of Vaud on research involving humans (Project No. 2018-01601). Among the 37 subjects, the demographic survey revealed only one person with extensive experience in VR, three with good experience with VR, and ten with no experience while others tried it only a few times.

## 2.2. Experimental protocol

### 2.2.1. Experimental environment

Participants sat in a comfortable chair and EEG signals were recorded throughout the experiment. The HTC Vive Pro Eye, a head-mounted display (HMD) with  $1440 \times 1600$  pixels per eye,  $110^\circ$  field of view and 90 Hz refresh rate, and a 120 Hz eye-tracking system with an accuracy of  $0.5^\circ$ – $1.1^\circ$  was used to monitor subjects' eye-movements. Bose QuietComfort 20 in-ear headphones with active noise canceling delivered a non-localized white noise. We captured participants' motion with 8 HTC Vive Trackers V2 (one to indicate the origin of the room in front of the chair where subjects sit, one on the subjects' chest, and three on each shoulder, elbow and hand). The participants also held an HTC Vive controller in their left hand to answer questions (figure 1(a)). Figure 1 and a supplementary video illustrate the general study design.

The virtual environment was a square room of  $6 \times 6 \times 3 \text{ m}^3$  with a chair in the middle. An avatar holding a tennis ball in its right hand was calibrated to co-locate the subjects' body. Haptic feedback was sustained by physically holding a real tennis ball while subjects observed a virtual tennis ball positioned in the same location. This maintained visuo-proprioceptive and tactile coherence between the real and virtual hands. The application was implemented using Unity 3D 2019.2.0f1. The participants' movements were reproduced through animation of the avatar using LimbIk from FinalIK<sup>11</sup>.

### 2.2.2. Experimental procedure

We performed the experiment in three groups. 14, 12 and 11 participants were in the first, second, and third groups, respectively. The experimental procedures of the first and second groups were divided into five phases (figure 1(e)); calibration, explanation, decoder-calibration, practice and distortion-adaptation. First, the motion capture suit, avatar, and EEG were calibrated (calibration phase). Then the participants performed the six trials with instructions (explanation phase). They then performed four runs of 75 trials, i.e. 50 trials without distortion and 25 trials with distortion (decoder-calibration phase). These data were used to train a personalized ErrP decoder. Each run used a different magnitude of distortion in a random order (3,5,7,10, see section 2.3).

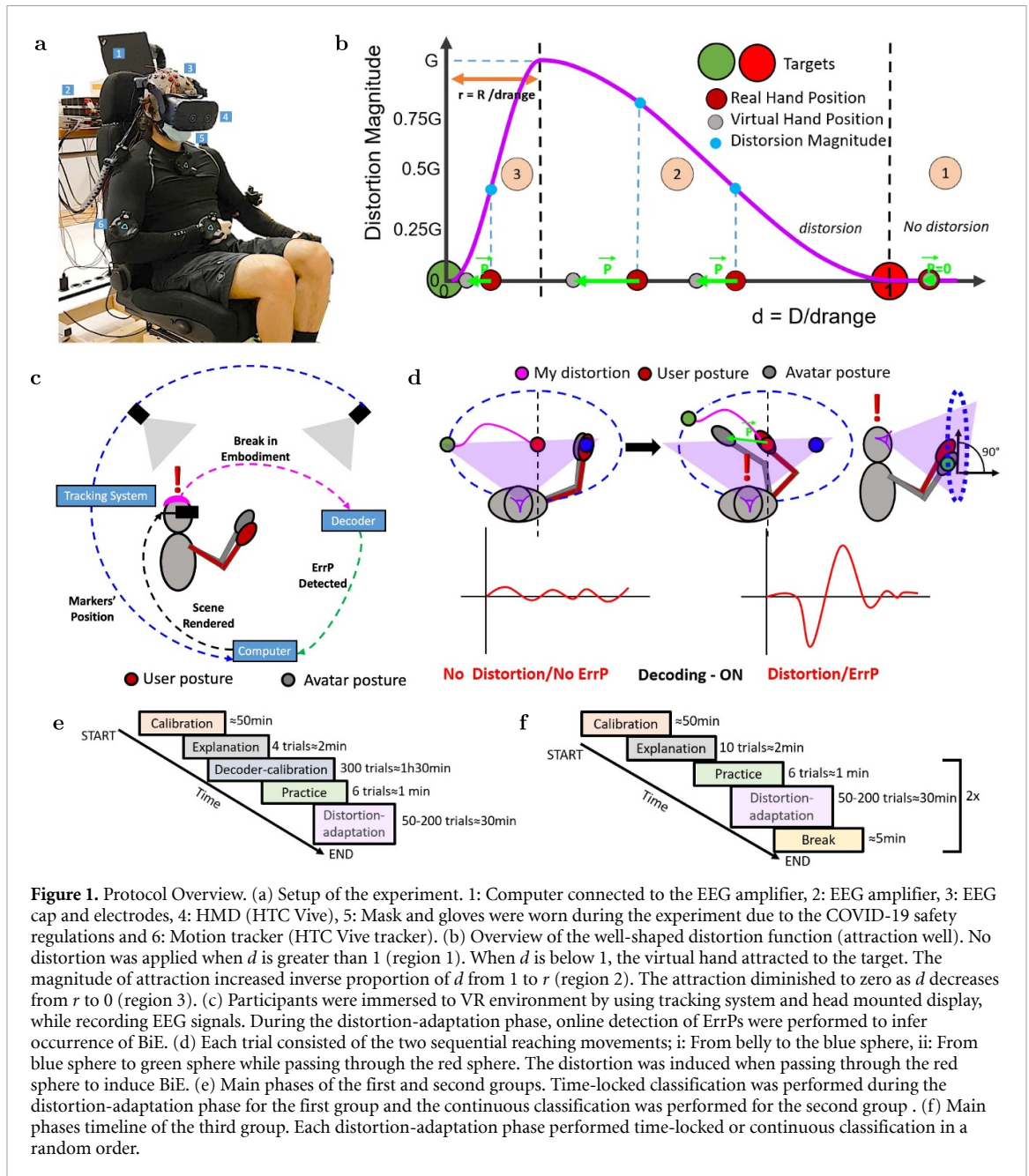
The participants performed the same task as in the decoder-calibration phase until convergence of the RL algorithm (distortion-adaptation phase, see section 2.5 for details). During the distortion-adaptation phase, the personalized decoder predicted the occurrence of BiE to customize the human-avatar mapping. Time-locked and continuous classification was performed during the distortion-adaptation phase for the first and second groups, respectively. In the third group (non-personalized decoder) the experiment was divided into the calibration, explanation, practice, and distortion-adaptation phases (figure 1(f)). The practice and distortion adaptation phases were repeated twice. Each distortion-adaptation phase was carried out with time-locked or continuous classification in a random order using the non-personalized decoder which was calibrated with all data in the decoder-calibration phase recorded from the first two groups.

### 2.2.3. Single-trial procedure

In both decoder-calibration and distortion-adaptation phases, each trial consisted of three times an arm reaching movement followed by two questions. Subjects started with their right hand on their belly holding a tennis ball. Three semitransparent spheres (blue, red, and green) and a red cross were displayed for each trial. Subjects were instructed to reach the first sphere (blue) to the right with the tennis ball and to remain inside at least 1 s to validate this first step. The validation progress was indicated in a gray circle, which became fully white once validated. Subjects then performed the avatar's arm reaching movement to the last sphere (green) while smoothly passing through the second sphere (red). The green sphere moved along a circular trajectory with a radius of 0.35 m. The distortion that helps reaching the green sphere (figure 1(b)) was activated when the avatar's hand was located within the red sphere. The distortion function (attraction well [27], section 2.3) was centered on the green target and expanded to the center of the red target (the same radius as the trajectory). Subjects had to stay inside the green target for at least 4 s to complete a trial. They were instructed to fixate their gaze on the red cross placed in front of them while doing the movement. If the gaze was not fixed on the red cross for 0.5 s, the trial restarted after showing a warning message to subjects.

After each reaching movement, participants answered to two yes/no questions by controlling a cursor; 'I felt that the virtual body moved exactly like me', and 'It felt that the virtual body was my own body.'. The first question indicates the subjective experience on conscious perception of the distorted avatar's arm reaching movement (perception of distortion, PoD) [33], and the second question indicates the presence of a

<sup>11</sup> [root-motion.com](http://root-motion.com).



BiE [1, 3]. After answering these questions, the full virtual scene reappeared at their initial position and the next trial started.

### 2.3. Attraction well

The distortion is designed to help participants reach and follow a moving target [1], and an excessive distortion induces a BiE [4]. The avatar's hand was first attracted towards the target until it reached the outer boundary of the moving target (i.e. a sphere slightly bigger than a tennis ball). Once the virtual hand was inside the moving target, the attraction was progressively reduced to zero until the avatar's hand arrived at the center of the target.

In our implementation, the distortion function started at the green sphere and extended towards the

red one, following the trajectory. Please note that the green sphere's path aligned precisely with the red sphere's position. To facilitate tracking a vertically moving green sphere with one hand, we calibrated the position of the red sphere for each subject. This calibration ensured that subjects did not have to fully extend their arms as the red sphere's position never exceeded 80% of their arm length from the shoulder position.

The magnitude of distortion was controlled based on the distance  $D$  between the 3D position of subject's hand  $\vec{P}_{real}$  and the 3D position of moving target  $\vec{P}_{target}$  of radius  $R$ , by the following equations;  $d = \frac{D}{d_{range}}$  and  $r = \frac{R}{d_{range}}$  where  $d_{range}$  is the distance range of the attraction force centered on the moving target.

The distortion magnitude was expressed as a function of the normalized distance  $d$  (figure 1(b) and (d)). For  $d > 1$ , no distortion occurred, hence the virtual hand position was identical to the real hand position. An attraction was enforced whenever  $d < 1$  thereby bringing the avatar hand closer to the target compared to the real hand.

The maximum magnitude of the attraction force was denoted as  $G$ . Then:

$$f(d) = \begin{cases} G \times (-2 \times (\frac{d}{r})^3 + 3 \times (\frac{d}{r})^2) & d \in [0, r] \\ G \times (2 \times (\frac{d-r}{1-r})^3 - 3 \times (\frac{d-r}{1-r})^2 + 1) & d \in [r, 1]. \end{cases} \quad (1)$$

Given the distortion value provided by the attraction profile  $f(d)$ , an attraction coefficient was computed  $1/(1+f(d))$  to build the distorted hand position  $\vec{P}_{\text{distorted}}$ , shown to subjects, from the knowledge of the current positions of the mobile target  $\vec{P}_{\text{target}}$  and the real hand  $\vec{P}_{\text{real}}$ . Then:

$$\vec{P}_{\text{distorted}} = \vec{P}_{\text{target}} + \left( \frac{1}{1+f(d)} \right) \times (\vec{P}_{\text{real}} - \vec{P}_{\text{target}}). \quad (2)$$

The magnitude of distortion  $f(d)$  being always positive, equation (2) ensured that the distorted hand position  $\vec{P}_{\text{distorted}}$  always lied in-between the current target position  $\vec{P}_{\text{target}}$  and the real hand position  $\vec{P}_{\text{real}}$ . Both the real and distorted positions coincided for the boundaries  $[0, 1]$  of the normalized distance  $d$ . The distortion was tuned based on  $R$ ,  $d_{\text{range}}$ , and  $G$  (referred to as the ‘distortion gain’). Based on the previous study [1], the following discrete distortion gains were used in the distortion-adaptation phase: (0, 0.25, 0.5, 0.75, 1, 1.25, 1.5, 1.75, 2, 2.25, 2.5, 2.75, 3, 4, 5, 7, 10). The last value covered the largest possible magnitude of distortion due to the limited field of view of the VR display.

## 2.4. EEG signal processing

### 2.4.1. EEG acquisition

We recorded 32 EEG and 3 electrooculogram (EOG) signals throughout the experiment at 512 Hz via three synchronized g.USBAmps (g.tec medical technologies, Austria). EEG active electrodes were located at AF3, AF4, F3, F1, Fz, F2, F4, FC3, FC1, FCz, FC2, FC4, C3, C1, Cz, C2, C4, CP3, CP1, CPz, CP2, CP4, P3, P1, Pz, P2, P4, PO3, POz, PO4, O1, O2 (10/10 international system), while the 3 EOG channels were placed above the nasion and below the outer canthi of the both eyes, forming a triangle. The ground electrode was placed on the forehead (AFz) and the reference electrode was on the left earlobe. The EEG and EOG signals were notch filtered at 50 Hz to eliminate the power noise. To reduce signal contamination, subjects were asked to stare at the cross and hold their head still when reaching the target. If the movements of their eyes or neck were above a certain threshold, the

trial was restarted to ensure the quality of the recorded signals.

Before the experiment, participants underwent 90 s of recording in which they performed three different kinds of eye movement, 30 s each; clockwise and counter-clockwise rolling of eyeballs, vertical and horizontal eye movements and repeated eye blinks. These data were subsequently used to compute coefficients to linearly remove EOG artifacts from EEG signals based on the autocovariance matrix of EEG and EOG signals [34, 35].

### 2.4.2. EEG preprocessing

EEG signals were band-pass filtered with a 4th order Butterworth filter with cutoff frequencies of [1 10] Hz. The signals were then segmented into epochs with a time window of [0.2 0.6] s relative to when the participants passed through the red sphere for each trial.

### 2.4.3. Time-locked classification of ErrPs

To build an ErrP decoder that monitors the presence or absence of ErrPs in real-time, we used only the data collected during the decoder-calibration phase. A personalized decoder was trained for participants in the first and second groups, while a non-personalized decoder was trained for the third group by accumulating all data in the first two groups’ decoder-calibration phase. All EEG epochs were concatenated to build the non-personalized classifier.

To enhance the signal-to-noise ratio (SNR) of ErrPs for the subsequent classification analysis, we applied a spatial filter based on canonical correlation analysis (CCA) [25, 36–38]. CCA-based spatial filters were linear transformations that maximize pairwise correlation between concatenated single-trial EEG epochs and averaged EEG epochs [39] (see [36] and supplementary figure 1 for details). The CCA spatial filter transformed the averaged ErrPs into a subspace that contained different deflections. Only the first three components were kept for further processing as described in previous studies [24, 36]. We extracted EEG amplitudes resampled at 64 Hz and Welch’s power spectral density between [4, 10] Hz with a step of 2 Hz as they have been shown to yield superior performance in other studies [24, 25, 40]. All computed features were concatenated and normalized within the range of [0, 1] via Min–Max normalization. From this feature vector  $\mathbf{x}$ , we computed the posterior probability of distortion  $p(\text{distortion}|\mathbf{x})$  using diagonal linear discriminant analysis (LDA):

$$p(\text{distortion}|\mathbf{x}) = \frac{1}{1 + \exp^{-(\mathbf{w}'\mathbf{x}+b)}} \quad (3)$$

where,  $\mathbf{w}$  and  $b$  are the parameters of the diagonal LDA.

For the first and the third group, in which a decoder was deployed to perform time-locked classification during distortion-adaptation phase, we used the theoretical decision threshold for binary classification, i.e. 0.5. Leave-one run-out cross validation was performed to validate the classification performance of the decoder-calibration phase for the first group.

#### 2.4.4. Continuous classification of ErrPs

For the second group that underwent the distortion-adaptation phase with a personalized decoder for continuous classification, the decoder was trained the same way as for the first group. In addition, we tuned the decision threshold. Leave-one run-out cross validation was performed to estimate the pseudo-continuous posterior probability at 32 Hz, i.e. from the onset to 0.6 s after reaching the green target. The maximum estimated posterior probability within a trial determined subjects' perception of BiEs. If it was above the decision threshold, the decoder detected BiEs during continuous reaching movements. The optimal operating point, which yielded the minimum number of false predictions, of the receiver operating characteristic (ROC) curve was determined as the decision threshold for the continuous classification.

For the third group, in which the non-personalized decoder was used during the distortion-adaptation phase, the optimal decision threshold for continuous classification was inferred for each participant based on the maximal posterior probabilities of the first four trials without distortion during the practice period (figure 1(f)) [23]. We performed leave-one subject-out cross-validation to compute the pseudo-continuous probabilities of the data collected in the first two groups' distortion-adaptation phase while avoiding the use of individual decoder-calibration data. The averaged maximum posterior probability of the first four trials during the practice period and the individual optimal threshold were used to model the sigmoid function that inferred the optimal decision threshold.

#### 2.4.5. Statistical analysis of ErrP decoding performance

In the decoder-calibration phase, the classification performance of the time-locked and continuous classification was measured as the area under the curve (AUC) and was statistically evaluated by a two-sample t-test. In the distortion-adaptation phase, ErrP-BCI output was compared with the answers to the PoD and BiE questions. Classification performance was measured as balanced classification accuracy, mean of true positive and true negative rate. Its chance level is 0.5. Paired t-test was used to evaluate the classification performance between the time-locked and continuous classification when using the non-personalized decoder, while a comparison of other

pairs was performed by a two-sample t-test. All  $p$ -values were Bonferroni corrected.

### 2.5. Reinforcement learning algorithm

We used a reinforcement learning algorithm that had been developed and validated in our previous study [27] to determine the pseudo-optimal distortion value from a set of multiple options. Each of the available choices corresponded to a distinct level of distortion gain, and the agents' actions were met with positive or negative rewards, depending on the magnitude of the distortion introduced. This method enabled us to effectively identify the most suitable distortion level based on the user's implicit feedback, the ErrP-BCI output.

The reinforcement learning algorithm combined upper-confidence-bound (UCB) exploration with the  $\epsilon$ -greedy policy.  $Q$ -values were initialized to zero for all actions [41]. The convergence of the  $Q$ -values, representing the expected rewards for each action, was monitored to determine the optimal threshold.

To adapt to the dynamic nature of the problem, parameters such as the exploration ratio  $\epsilon$  and the learning rate  $\alpha$  decayed over time. The study carefully selected decay rates through a prior grid search. The algorithm also had termination conditions in place to avoid running indefinitely (15 unchanged iterations after the 35th trial and stopped if it reached 200 iterations). More details can be found in our previous study [27].

### 2.6. Psychometric function

We computed the PoD and BiE thresholds of each subject based on the answer to the first and second questions during the distortion-adaptation phase, respectively. We used a psychometric function [42, 43] to calculate each threshold (supplementary figure 4). The PoD threshold is the magnitude of distortion in which subjects detected the distortion 50% of times, while the BiE threshold corresponded to an approximation of the minimum magnitude of distortion in which subjects rejected the virtual body as their body at 50% of times.

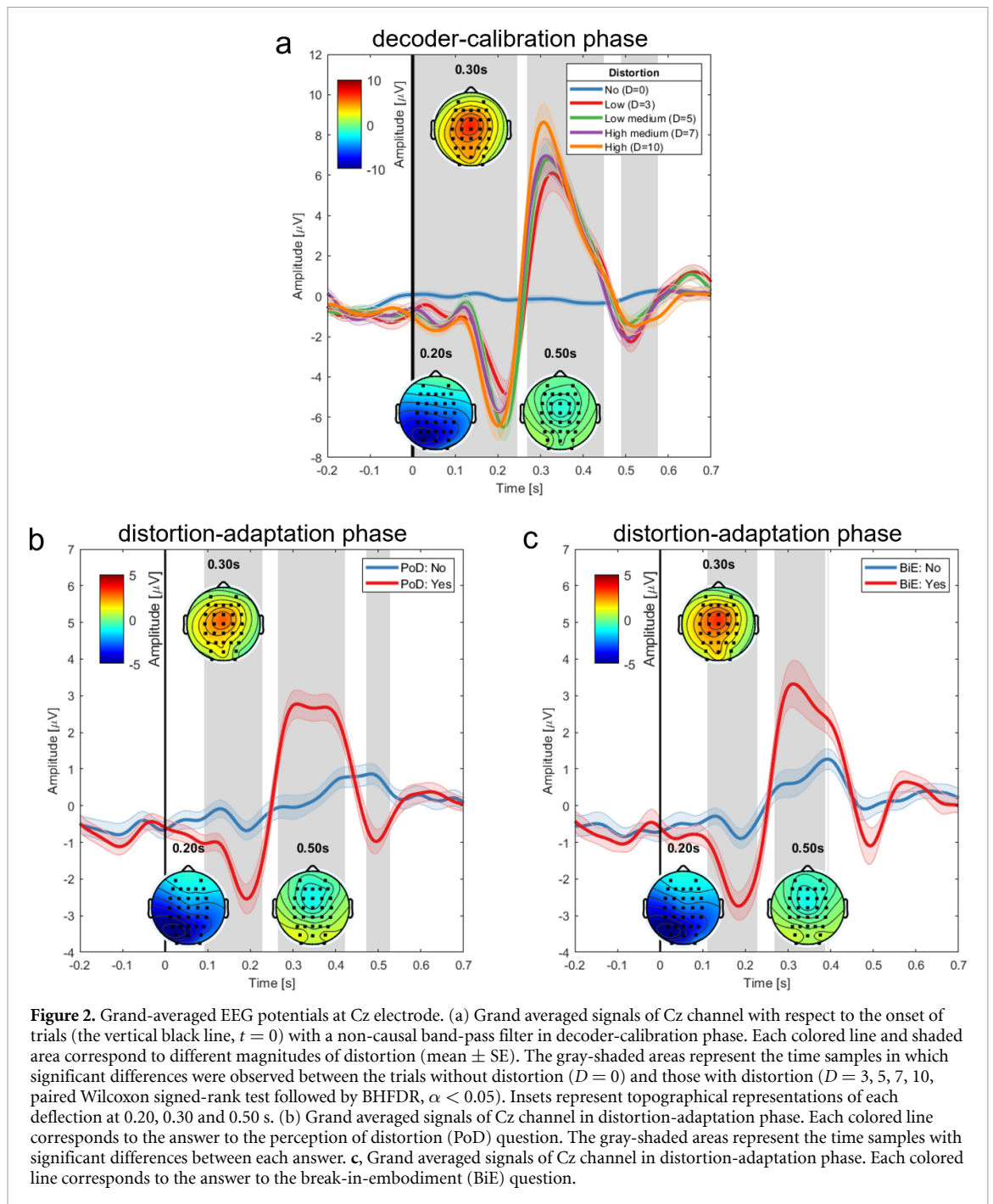
### 2.7. Statistical analysis of the thresholds

To evaluate whether PoD, BiE and RL thresholds were comparable, a one-way repeated measures ANOVA was performed for each decoding conditions, i.e. time-locked and continuous classification with personalized and non-personalized decoders.

## 3. Results

### 3.1. Electrophysiological results

We observed sequential negative, positive, and negative deflections after the onset of distortions in the

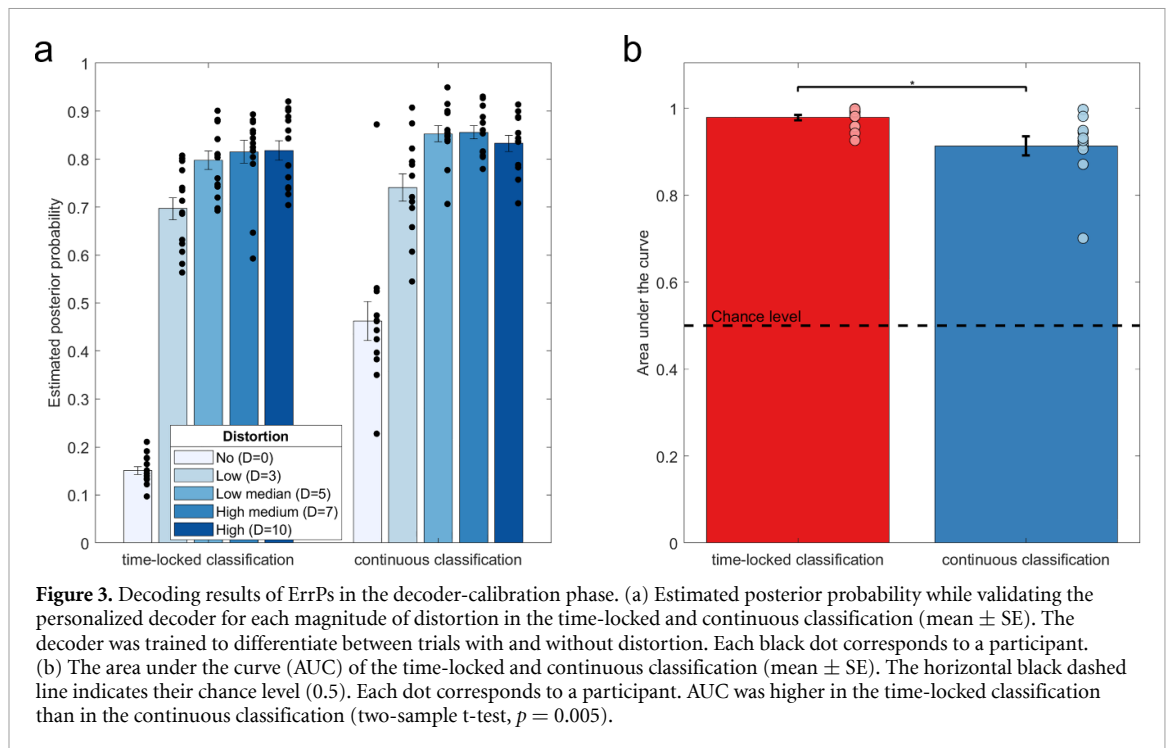


decoder-calibration phase ( $p < 0.05$ , paired Wilcoxon signed-rank test followed by Benjamini–Hochberg false discovery correction (BHFD), figure 2(a) [44, 45]). These deflections were present throughout the decoder-calibration phase (supplementary figure 2). These deflections were strongly elicited from the parietal and the central area of the brain (figure 2(a)). On the other hand, EEG potentials remained mostly flat around the onset without distortion. Similarly, in the distortion-adaptation phase, sequential deflections were observed when participants perceived distortion (figure 2(b)) and when participants experienced BiE

(figure 2(c)), and these deflections were attenuated when they did not.

### 3.2. Decoding results

In the decoder-calibration phase, the estimated posterior probability in the trials without distortion was lower than that with distortion (figure 3(a)). The posterior probability increased progressively over the magnitude of distortion for both time-locked (Spearman  $r = 0.72$ ,  $p < 0.001$ ) and continuous classification ( $r = 0.58$ ,  $p < 0.001$ ). The AUC was  $0.97 \pm 0.007$  (mean  $\pm$  SE) for time-locked, and 0.89



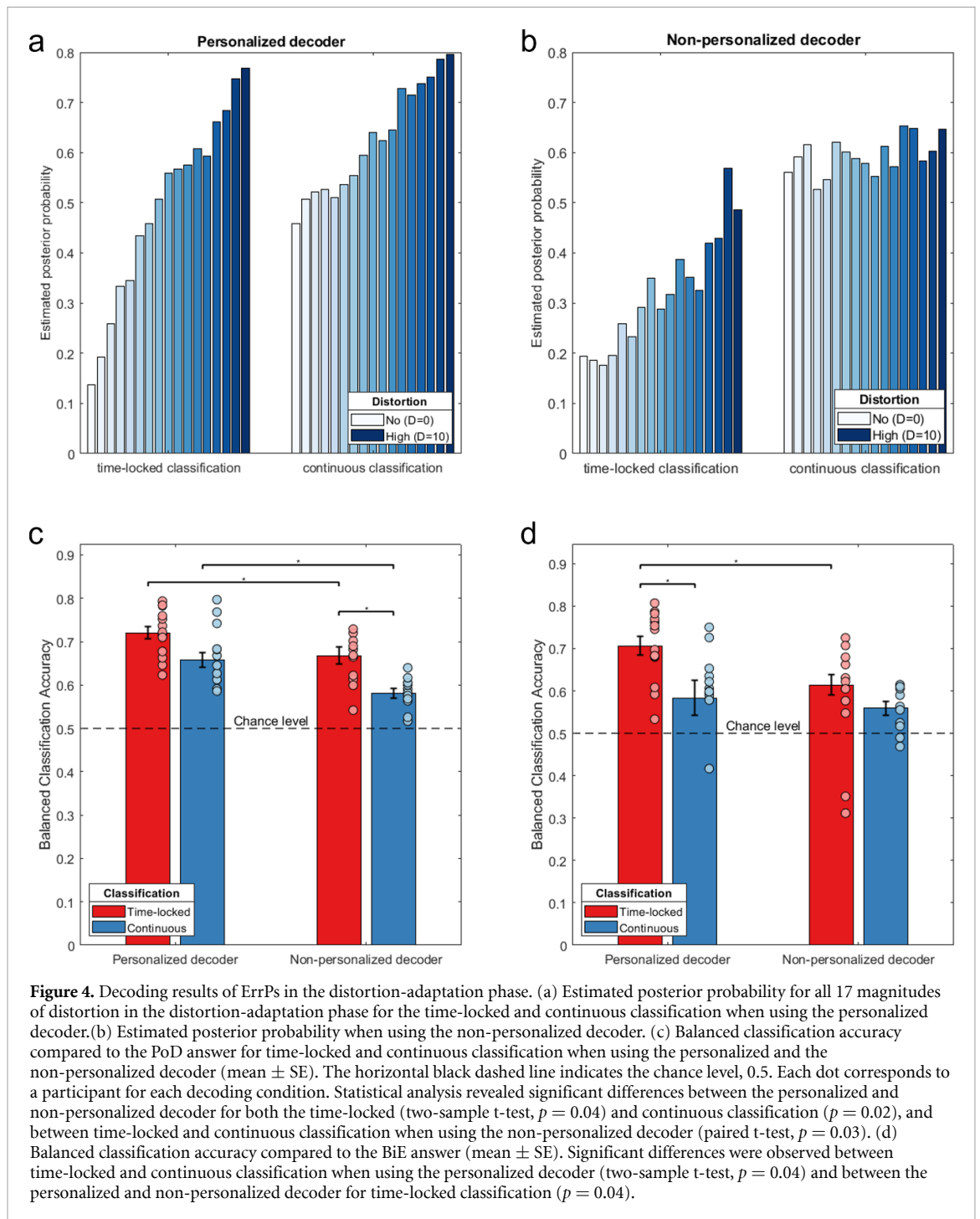
$\pm 0.029$  for continuous classification (figure 3(b)). They were above the chance level (0.5), but the continuous classification performance was significantly lower than the time-locked classification performance (two-sample t-test,  $p = 0.005$ , figure 3(b)). Please note that our validation procedure, leave-one run-out cross validation, did not positively bias the ErrP-BCI classification performance (supplementary figure 3).

Similarly to the decoder-calibration phase, the estimated posterior probability progressively increased over the magnitude of distortion in the distortion-adaptation phase for both time-locked (Spearman  $r = 0.79$ ,  $p < 0.001$ ) and continuous classification ( $r = 0.62$ ,  $p < 0.001$ , figure 4(a) and supplementary figure 4). Despite its consistent trend over the magnitude of distortion, the probability was differentiated between time-locked and continuous classification, especially in trials with no or small distortion. Further, progressive increase in posterior probability was also observed when using the non-personalized decoder for both time-locked ( $r = 0.62$ ,  $p < 0.001$ ) and continuous classification ( $r = 0.29$ ,  $p < 0.001$ , figure 4(b)). The posterior probability range was smaller when using the non-personalized decoder compared to the corresponding classification approach using the personalized decoder.

In the distortion-adaptation phase, all four classification conditions outperformed the chance level as

measured in balanced classification accuracy for both PoD (figure 4(c)) and BiE questions (figure 4(d)). For both questions, classification performance was highest for the time-locked classification with the personalized decoder. On the other hand, it was the lowest for the continuous classification with the non-personalized decoder. When comparing ErrP-BCI outputs with the PoD question, the statistical differences were observed between the personalized and non-personalized decoder for both the time-locked (two-sample t-test,  $p = 0.04$ ) and continuous classification (two-sample t-test,  $p = 0.02$ ), and between time-locked and continuous classification when using the non-personalized decoder (paired t-test,  $p = 0.03$ ). There were no statistical differences between time-locked and continuous classification when using the personalized decoder (two-sample t-test,  $p = 0.16$ ). For the BiE question, the difference was observed between time-locked and continuous classification when using the personalized decoder (two-sample t-test,  $p = 0.04$ ) and between the personalized and non-personalized decoder for the time-locked classification (two-sample t-test,  $p = 0.04$ ). On the other hand, no differences were observed between time-locked and continuous classification when using the non-personalized decoder (paired t-test,  $p = 1.0$ ) and between the personalized and non-personalized decoder for continuous classification (two-sample t-test,  $p = 0.30$ ).





### 3.3. Behavioral and reinforcement learning results

The PoD and BiE rates increased progressively over the magnitude of distortion (Spearman  $r = 0.68$ ,  $p < 0.001$  for PoD,  $r = 0.49$ ,  $p < 0.001$  for BiE, figure 5(a)). However, they showed slightly different modulations from each other. PoD rate showed a more rapid increase relative to BiE rate.

The RL threshold was between the PoD and BiE thresholds when using the personalized decoder (figure 5(b) and table 1). Statistical analysis did not reveal differences between the three thresholds (two

one-way repeated measures ANOVAs,  $F(2, 26) = 1.61$ ,  $p = 0.219$  for time-locked, and  $F(2, 22) = 2.52$ ,  $p = 0.103$  for continuous classification). On the other hand, when the non-personalized decoder was used, the RL threshold was higher than the PoD and BiE thresholds (figure 5(c)). The statistical analysis did not reveal significant differences between the three thresholds (two one-way repeated measures ANOVAs,  $F(2, 20) = 3.22$ ,  $p = 0.061$  for time-locked, and  $F(2, 20) = 1.06$ ,  $p = 0.364$  for continuous classification).

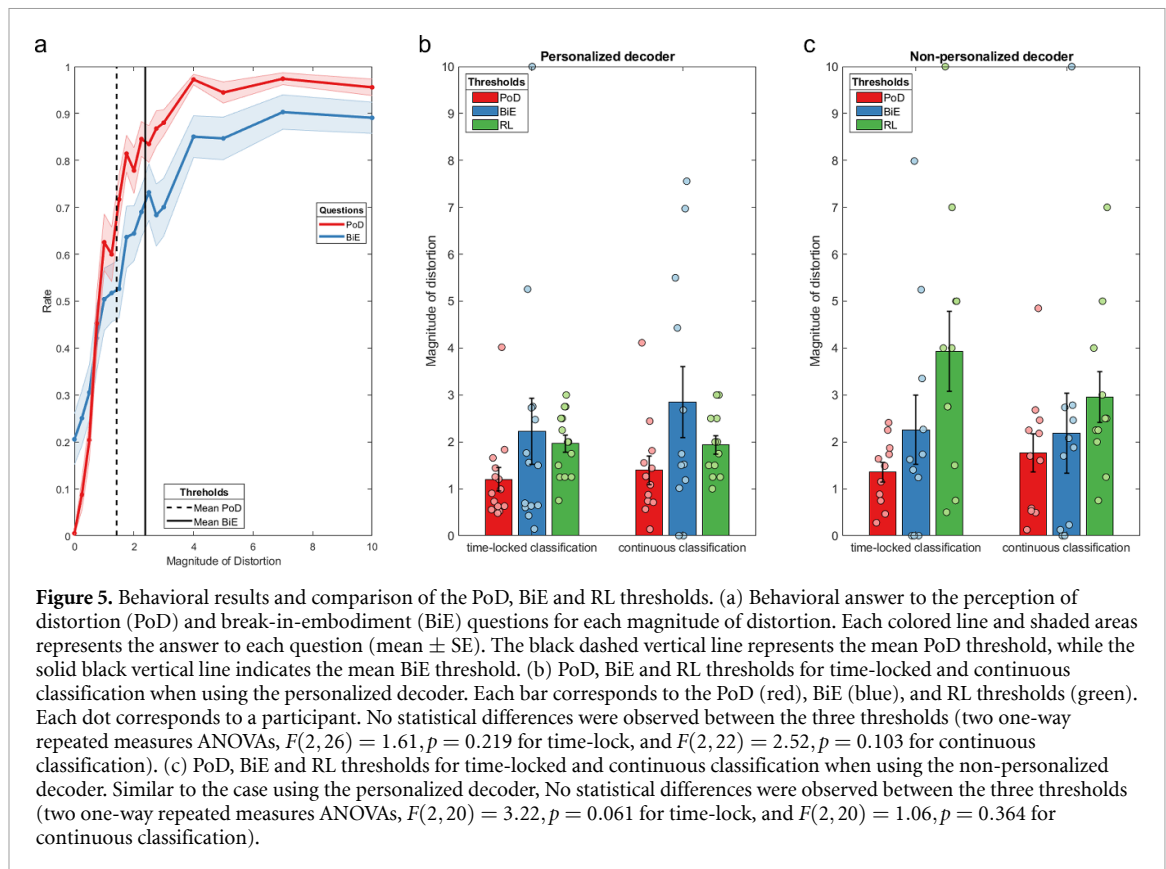


**Table 1.** PoD, BiE and RL thresholds and the number of trials performed in the distortion-adaptation phase for each decoding condition (mean  $\pm$  SE).

	Personalized decoder		Non-personalized decoder	
	Time-locked	Continuous	Time-locked	Continuous
PoD threshold	1.20 $\pm$ 0.25	1.40 $\pm$ 0.30	1.36 $\pm$ 0.21	1.77 $\pm$ 0.41
BiE threshold	2.23 $\pm$ 0.70	2.84 $\pm$ 0.76	2.26 $\pm$ 0.74	2.18 $\pm$ 0.85
RL threshold	1.96 $\pm$ 0.19	1.94 $\pm$ 0.20	3.93 $\pm$ 0.85	2.95 $\pm$ 0.54
Number of trials	70 $\pm$ 6	77 $\pm$ 6	84 $\pm$ 12	75 $\pm$ 5

## 4. Discussion

We have presented a novel BCI-VR closed-loop system integrated in an immersive interactive system that allows seamless adjustment of the mapping between the users' actual movements and their avatar for the benefit of interaction in VR. The present study demonstrated the possibility of adjusting the magnitude of distortion through an implicit ErrP-BCI feedback. The ErrP-BCI decoding output was exploited as reward signals to adjust the magnitude of distortion to perform the avatar's arm reaching movement while preserving the SoE, thus maintaining their virtual experiences. The proposed BCI-VR closed-loop system is beneficial for customizing the human-avatar mapping based on user's brain activity, which has been limited to users' explicit feedback to date. In order to compensate for the limited signal-to-noise ratio of the BCI output, we incorporated the RL algorithm to identify the optimal magnitude of distortion. The proposed approach successfully

achieved the pseudo-optimal magnitude of distortion and demonstrated its ability to fine-tune levels of assistance for each participant while avoiding degradation of virtual experiences due to BiEs.

Specifically, as shown in previous studies [1, 33, 46] and illustrated in figure 5(a), participants maintained a high level of embodiment even when they could perceive the distortion. In effect, we show that there are three distinct stages of cognitive processing before participants notice and then reject a movement distortion of their avatar. In the first stage, for very low distortions, they are not able to perceive the distortion. In the second stage, between the PoD and the BiE thresholds, participants are still experiencing a strong embodiment for their avatar despite being able to consciously evaluate that the avatar's arm reaching movement is distorted. In the third stage, beyond the BiE threshold, participants reject the distortion as an error of the system, provoking an ErrP that the BCI system can detect. The threshold computed by our BCI-RL approach successfully computed the

pseudo-optimal threshold to be in between the PoD and the BiE thresholds when deploying the personalized ErrP decoder. Importantly, these RL thresholds were nearly identical to those obtained with explicit feedback ( $1.93 \pm 0.23$  [mean  $\pm$  SE]) [27] (table 1). Thus, thanks to our individually customized distortion magnitude, users performed the reaching task without affecting their experience of embodiment for their avatar.

As opposed to previous works that evaluated the user's brain response at given time points (e.g. after the executions of a movement by an avatar) [19, 20, 47], we performed continuous classification of ErrPs during avatar-based interactions and used the ErrP-BCI decoding outputs to customize the human-avatar mapping. Replacing time-locked by continuous classification of ErrPs is a challenge for BCI due to the uncertainty of EEG signals, but a necessary step for applying it to VR interaction, as users continuously interact with their embodied avatar. Although a previous work showed the customization of robot trajectories through continuous ErrP classification [25], their task did not involve varying magnitudes in erroneous interactions. A recent study [24] revealed the scalability of the ErrP-BCI decoding outputs over the magnitude of errors, and posed the challenge of decoding ErrPs induced by small errors. Critically, our experimental protocol did not include trials with a small magnitude of distortions in the decoder-calibration phase. Nevertheless, our BCI-VR closed-loop system using a personalized decoder successfully classified trials with small distortions and customized the human-avatar mapping, allowing one to maintain embodiment for their avatar.

Furthermore, we also evaluated to what extent the decoder trained with multiple participants generalizes to a new group of participants (non-personalized decoder) [48, 49]. The decoding performance degraded both in time-locked and continuous classification compared to the personalized decoder (figures 4(c) and (d)). The RL threshold obtained with the non-personalized decoder did not reveal significant differences from the PoE nor BiE threshold, while being higher than them. These RL thresholds were also higher than those identified with explicit feedback [27] (table 1). Notably, when the non-personalized decoder was used, participants saved about 90 mins as data collection to calibrate the personalized decoder was omitted. Thus, they were still able to receive implicit BCI feedback immediately after the instruction to customize their human-avatar mapping. Although the non-personalized decoder showed degraded performance (figures 4(c) and (d)), our analysis revealed a progressive increase in the output of the non-personalized decoder output for both time-locked and continuous classification over the magnitude of distortions, but limited to smaller ranges (figures 4(a) and (b)). This suggests the importance of calibrating

the decision threshold when deploying the non-personalized decoder for both time-locked and continuous classification and also the need to update the decoder to increase the range of posterior probabilities. These procedures may further improve precision of RL thresholds when using a non-personalized decoder.

One of the limitations of the present study is the relatively specific human-avatar mapping and BCI algorithms. For example, subjects were instructed to fix their gazes and head movements to preserve EEG signals from possible muscle contamination, and they performed repetitive reaching actions to collect enough data to build a personalized decoder and calibrate their interaction. In an ideal scenario, we expect participants to move freely without repetitive actions, while the BCI-VR closed-loop system implicitly calibrates their human-avatar mapping without the need for collecting data for building a personalized decoder.

In summary, this study demonstrated the possibility and showed the benefits of online adaptation of the human-avatar mapping during VR experiences, without asking explicitly or interrupting the interaction. Although the RL threshold obtained with a non-personalized decoder was not between PoD and BiE thresholds, the decoder may be adaptively updated in an experiment consisting of multiple sessions [24]. Thus, it would be crucially important to test our BCI-VR system over longitudinal sessions because one could speculate that users would increase their sensitivity to perceive visuo-proprioceptive conflicts and become more susceptible to BiE over time. Future studies may include use of the VR system over multiple sessions and evaluate their PoD, BiE and RL threshold, with the possibility to change over sessions while updating the decoder. With increasing involvement of full-body interaction in immersive VR commercial products, BCI-VR systems would be beneficial for optimizing the human-avatar mapping, allowing to maintain an engaging avatar-based interaction and a compelling immersive experience while detecting when users notice a problem and seamlessly correcting it.

## Data availability statement

The data that support the findings of this study are openly available at the following URL/DOI: <https://zenodo.org/records/8111105>.

## Acknowledgments

This work was supported by the Swiss National Science Foundation (Project 'Immersive Embodied Interactions', 200020.178790), the Hasler Foundation, Switzerland, and by the Swiss National Center of Competence in Research in Robotics (NCCR).

## ORCID iDs

Fumiaki Iwane  <https://orcid.org/0000-0002-9659-4127>

Thibault Porssut  <https://orcid.org/0000-0002-6691-1427>

Olaf Blanke  <https://orcid.org/0000-0002-9745-3983>

Ricardo Chavarriaga  <https://orcid.org/0000-0002-8879-2860>

José del R Millán  <https://orcid.org/0000-0001-5819-1522>

Bruno Herbelin  <https://orcid.org/0000-0003-4570-5146>

Ronan Boulic  <https://orcid.org/0000-0001-9176-6877>

## References

- [1] Porssut T, Herbelin B and Boulic R 2019 Reconciling being in-control vs. being helped for the execution of complex movements VR *IEEE Conf. on Virtual Reality and 3D User Interfaces VR* pp 529–37
- [2] Kilteni K, Groten R and Slater M 2012 The sense of embodiment in virtual reality *Presence Teleoperators Virtual Environ.* **21** 373–87
- [3] Kokkinara E and Slater M 2014 Measuring the effects through time of the influence of visuomotor and visuotactile synchronous stimulation on a virtual body ownership illusion *Perception* **43** 43–58
- [4] Porssut T, Iwane F, Chavarriaga R, Blanke O, Millán J d R, Boulic R and Herbelin B 2023 EEG signature of breaks in embodiment in VR *PLoS One* **18** 1–13
- [5] Falkenstein M, Hohnsbein J, Hoormann J and Blanke L 1991 Effects of crossmodal divided attention on late ERP components. II. Error processing in choice reaction tasks *Electroencephalogr. Clin. Neurophysiol.* **78** 447–55
- [6] Gehring W J, Goss B, Coles M G H, Meyer D E and Donchin E 1993 A neural system for error detection and compensation *Psychol. Sci.* **4** 385–90
- [7] Holroyd C B and Coles M G H 2002 The neural basis of human error processing: reinforcement learning, dopamine and the error-related negativity *Psychol. Rev.* **109** 679–709
- [8] Pezzetta R, Nicolardi V, Tidoni E and Aglioti S M 2018 Error, rather than its probability, elicits specific electrocortical signatures: a combined EEG-immersive virtual reality study of action observation *J. Neurophysiol.* **120** 1107–18
- [9] Spinelli G, Tieri G, Pavone E F and Aglioti S M 2018 Wronger than wrong: graded mapping of the errors of an avatar in the performance monitoring system of the onlooker *NeuroImage* **167** 1–10
- [10] Pavone E F, Tieri G, Rizza G, Tidoni E, Grisoni L and Aglioti S M 2016 Embodying others in immersive virtual reality: electro-cortical signatures of monitoring the errors in the actions of an avatar seen from a first-person perspective *J. Neurosci.* **36** 268–79
- [11] Raz G, Gurevitch G, Vaknin T, Aazamy A, Gefen I, Grunstein S, Azouri G and Goldway N 2019 Electroencephalographic evidence for the involvement of mirror-neuron and error-monitoring related processes in virtual body ownership *NeuroImage* **207** 116351
- [12] Padrao G, Gonzalez-Franco M, Sanchez-Vives M V, Slater M and Rodriguez-Fornells A 2016 Violating body movement semantics: neural signatures of self-generated and external-generated errors *NeuroImage* **124** 147–56
- [13] Si-Mohammed H, Lopes-Dias C, Duarte M, Argelaguet F, Jeunet C, Casiez G, Müller-Putz G R, Lécuyer A and Scherer R 2020 Detecting system errors in virtual reality using EEG through error-related potentials *IEEE Conf. on Virtual Reality and 3D User Interfaces (VR)* pp 653–61
- [14] Steinhauser R, Wirth R, Kunde W, Janczyk M and Steinhauser M 2018 Common mechanisms in error monitoring and action effect monitoring *Cogn. Affective Behav. Neurosci.* **18** 1159–71
- [15] Rabbitt P A 1966 Errors and error correction in choice-response tasks *J. Exp. Psychol.* **71** 264
- [16] Chang A, Chen C C, Li H H and Li C S R 2014 Event-related potentials for post-error and post-conflict slowing *PLoS One* **9** e99909
- [17] Chavarriaga R and Millán J d R 2010 Learning from EEG error-related potentials in noninvasive brain-computer interfaces *IEEE Trans. Neural Syst. Rehabil. Eng.* **18** 381–8
- [18] Ferrez P and Millán J d R 2008 Error-related EEG potentials generated during simulated brain-computer interaction *IEEE Trans. Biomed. Eng.* **55** 923–9
- [19] Iturrate I, Chavarriaga R, Montesano L, Minguez J and Millán J d R 2015 Teaching brain-machine interfaces as an alternative paradigm to neuroprosthetics control *Sci. Rep.* **5** 13893
- [20] Salazar-Gomez A F, DelPreto J, Gil S, Guenther F H and Rus D 2017 Correcting robot mistakes in real time using EEG signals *IEEE Int. Conf. on Robotics and Automation* pp 6570–7
- [21] Chavarriaga R, Sobolewski A and Millán J d R 2014 Errare machinale est: the use of error-related potentials in brain-machine interfaces *Front. Neurosci.* **8** 208
- [22] Dias C L, Sburlea A I and Müller-Putz G R 2018 Masked and unmasked error-related potentials during continuous control and feedback *J. Neural Eng.* **15** 036031
- [23] Lopes-Dias C, Sburlea A I, Breitegger K, Wyss D, Drescher H, Wildburger R and Müller-Putz G R 2021 Online asynchronous detection of error-related potentials in participants with a spinal cord injury using a generic classifier *J. Neural Eng.* **18** 046022
- [24] Iwane F, Sobolewski A, Chavarriaga R and Millán J d R 2023 EEG error-related potentials encode magnitude of errors and individual perceptual thresholds *iScience* **26** 107524
- [25] Batzianoulis I, Iwane F, Wei S, Correia C G P R, Chavarriaga R, Millán J d R and Billard A 2021 Customizing skills for assistive robotic manipulators, an inverse reinforcement learning approach with error-related potentials *Commun. Biol.* **4** 1406
- [26] Iwane F, Billard A and Millán J d R 2023 Inferring individual evaluation criteria for reaching trajectories with obstacle avoidance from EEG signals *Sci. Rep.* **13** 20163
- [27] Porssut T, Hou Y, Blanke O, Herbelin B and Boulic R 2022 Adapting virtual embodiment through reinforcement learning *IEEE Trans. Vis. Comput. Graph.* **28** 3193–205
- [28] Jauregui D A G, Argelaguet F, Olivier A H, Marchal M, Multon F and Lécuyer A 2014 Toward 'pseudo-haptic avatars': modifying the visual animation of self-avatar can simulate the perception of weight lifting *IEEE Trans. Vis. Comput. Graph.* **20** 654–61
- [29] Azmandian M, Hancock M, Benko H, Ofek E and Wilson A D 2016 Haptic retargeting: dynamic repurposing of passive haptics for enhanced virtual reality experiences *Conf. on Human Factors in Computing Systems* pp 1968–79
- [30] Burns E, Razaque S and Whitton M 2007 MACBETH: management of avatar conflict by employment of a technique hybrid *Int. J. Virtual Real.* **6** 11–20
- [31] Bowman D A and Hodges L F 1997 An evaluation of techniques for grabbing and manipulating remote objects in immersive virtual environments *Symp. on Interactive 3D Graphics* pp 35–38
- [32] Porssut T, Blanke O, Herbelin B and Boulic R 2022 Reaching articular limits can negatively impact embodiment in virtual reality *PLoS One* **17** e0255554
- [33] Galvan D H, Boulic R, Salomon R, Blanke O and Herbelin B 2018 Self-attribution of distorted reaching movements in immersive virtual reality *Comput. Graph.* **76** 142–52

- [34] Schlögl A, Keinrath C, Zimmermann D, Scherer R, Leeb R and Pfurtscheller G 2007 A fully automated correction method of EOG artifacts in EEG recordings *Clin. Neurophysiol.* **118** 98–104
- [35] Iwane F, Iturrate I, Chavarriaga R and Millán J d R 2021 Invariability of EEG error-related potentials during continuous feedback protocols elicited by erroneous actions at predicted or unpredicted states *J. Neural Eng.* **18** 046044
- [36] Spüler M, Walter A, Rosenstiel W and Bogdan M 2014 Spatial filtering based on canonical correlation analysis for classification of evoked or event-related potentials in EEG data *IEEE Trans. Neural Syst. Rehabil. Eng.* **22** 1097–103
- [37] Iwane F, Chavarriaga R, Iturrate I and Millán J d R 2016 Spatial filters yield stable features for error-related potentials across conditions *IEEE Int. Conf. on Systems, Man and Cybernetics* pp 661–6
- [38] Spüler M 2017 Spatial filtering of EEG as a regression problem *7th Graz Brain-Computer Interface Conf.* (<https://doi.org/10.3217/978-3-85125-533-1-84>)
- [39] Hotelling H 1936 Relations between two sets of variates *Biometrika* **28** 321–77
- [40] Zhang H, Chavarriaga R, Khaliliardali Z, Gheorghe L, Iturrate I and Millán J d R 2015 EEG-based decoding of error-related brain activity in a real-world driving task *J. Neural Eng.* **12** 066028
- [41] Sutton R S and Barto A G 1998 *Reinforcement Learning: An Introduction* (MIT Press)
- [42] Lecuyer A, Coquillart S, Kheddar A, Richard P and Coiffet P 2000 Pseudo-haptic feedback: can isometric input devices simulate force feedback? *IEEE Virtual Reality* pp 83–90
- [43] Klein S A 2001 Measuring, estimating and understanding the psychometric function: a commentary *Percept. Psychophys.* **63** 1421–55
- [44] Hajcak G, McDonald N and Simons R F 2003 To err is autonomic: error-related brain potentials, ANS activity and post-error compensatory behavior *Psychophysiology* **40** 895–903
- [45] Gehring W, Liu Y, Orr J and Carp J 2012 The error-related negativity (ERN/Ne) *The Oxford Handbook of Event-Related Potential Components* (Oxford University Press) (<https://doi.org/10.1093/oxfordhb/9780195374148.013.0120>)
- [46] Debarba H G, Perrin S and Boulic R 2018 Perception of redirected pointing precision in immersive virtual reality *IEEE Conf. on Virtual Reality and 3D User Interfaces (VR)*
- [47] Ehrlich S K and Cheng G 2018 Human-agent co-adaptation using error-related potentials *J. Neural Eng.* **15** 066014
- [48] Lopes-Dias C, Sburlea A I and Müller-Putz G R 2020 A generic error-related potential classifier offers a comparable performance to a personalized classifier *42nd Annual Int. Conf. IEEE Engineering in Medicine & Biology Society* pp 2995–8
- [49] Bhattacharyya S, Konar A, Tibarewala D N and Hayashibe M 2017 A generic transferable EEG decoder for online detection of error potential in target selection *Front. Neurosci.* **11** 226